Material-point simulation of cavity collapse under shock

2007 J. Phys.: Condens. Matter 19 326212

(http://iopscience.iop.org/0953-8984/19/32/326212)

IOP PUBLISHING JOURNAL OF PHYSICS: CONDENSED MATTER

J. Phys.: Condens. Matter **19** (2007) 326212 (11pp) doi:10.1088/0953-8984/19/32/326212

Material-point simulation of cavity collapse under shock

Aiguo Xu, X F Pan, Guangcai Zhang and Jianshi Zhu

Laboratory of Computational Physics, Institute of Applied Physics and Computational Mathematics, PO Box 8009-26, Beijing 100088, People's Republic of China

E-mail: Xu_Aiguo@iapcm.ac.cn

Received 16 April 2007, in final form 9 June 2007
Published 16 July 2007
Online at stacks.iop.org/JPhysCM/19/326212

Abstract

The collapse of cavities under shock is a key problem in various fields ranging from erosion of material, ignition of explosive, to sonoluminescence, etc. We study such processes using the material-point method developed recently in the field of solid physics. The main points of the research include the relations between the symmetry of collapsing and the strength of shock, and other coexisting interfaces, as well as hydrodynamic and thermal–dynamic behaviours ignored by the pure fluid models. In the case with strong shock, we study the procedure of jet creation in the cavity; in the case with weak shock, we found that the cavity cannot be collapsed completely by the shock and that the cavity may collapse in a nearly isotropic way. The history of collapsing significantly influences the distribution of 'hot spots' in the shocked material. The change in symmetry of collapsing is investigated. Since we use the Mie–Grüneisen equation of state and the effects of strain rate are not taken into account, the behaviour is the same if one magnifies the spatial and temporal scales in the same way.

1. Introduction

The first work on cavitation phenomena dates back to 1894, when Reynolds observed such a phenomenon in water flowing through a tube with a local constriction [1]. A few years later, very destructive actions of cavitation in some industrial systems, such as steamship propellers, hydroturbines, etc, were found [2–5]. Then, it was addressed and discussed under other various backgrounds [6–9], for example, hot spots in explosives from which reaction ensues [5], the recent observation of sonoluminescence [10], etc. Now, controlled cavitation erosion is regarded as a powerful tool for modern technologies like steam/wet laser cleaning [11], effective salmonella destruction [12], and treatment for kidney stones [13]. Among the publications on cavitation in the literature, most of them resorts to experiments, then theoretical calculations, and only a small portion rely on numerical simulations. The physical models used

can be put into two categories, fluidic ones and solid ones. The numerical tools for the former are hydrodynamic codes [14], and for the latter are molecular dynamics (MD) [15–17] and the finite-element method [18].

Most of the analyses here are based on fluidic models. The most elegant mathematical description of bubble motion is one-dimensional [5]. It has long been observed that a tongue of liquid may be projected into a bubble under gravity and a tongue of metal may be projected into a cavity under shock, which confirm that one primary mechanism of erosion by cavitation is mechanical [3, 19]. The observation of such an asymmetric collapse stimulates the question as to what kind of boundary conditions give rise to it. The first kind of attempt simply considers it to be a geometric flow effect of the boundary. The second one regards it as the spallation of one surface towards the other by an incident shock, where the upstream face converges towards the stationary downstream one in the jet. In either of the two cases, the aspherical collapse implies that an impulse is applied, typically by an impact jet, to the surrounding fluid or solid in contact [5].

From the numerical simulation side, fluidic models of cavitation in metals ignore some important characteristics of the solid, such as plastic strain, hardening, and properties relevant to the deformation history. At the same time, the material under investigation is highly distorted during the collapsing of cavities. This causes severe problems in computational modelling of such a process. It is well known that the Eulerian description is not convenient for tracking interfaces. When the Lagrangian formulation is used to describe problems with large displacement and large strain, the original element mesh becomes distorted so significantly that the mesh has to be re-zoned to restore the proper shapes of the elements. The state fields of mass density, velocities and stresses must be mapped from the distorted mesh to the newly generated one. This mapping procedure is not a straightforward task, and it introduces errors. To treat large distortions problems, several mixed methods have been developed recently. Among these methods, the material-point method (MPM), introduced originally in fluid dynamics by Harlow *et al* [20] and extended to solid mechanics by Burgess *et al* [21], overcomes the above-mentioned concerns. At each time step, the calculations consist of two parts: a Lagrangian part and a convective one. First, the computational mesh deforms with the body, and is used to determine the strain increment, and the stresses in what follows. Then, the new position of the computational mesh is chosen (it may be the previous one), and the velocity field is mapped from the particles to the mesh nodes. Nodal velocities are determined using the equivalence of momentum calculated for the particles and for the computational grid. The method not only takes advantage of both the Lagrangian and Eulerian algorithms but it makes it possible to avoid their drawbacks as well. In this work we use an improved MPM [22] to investigate the collapse of cavities in shocked metal.

The remainder of the paper is organized as follows. Section 2 describes briefly the numerical scheme. Section 3 shows the physical model and section 4 presents simulation results. Section 5 provides the conclusions.

2. The material-point method

The material-point method [21] is a particle method, where the continuum bodies are discretized with N_p material particles. Each material particle carries the information of position $\mathbf{x}_p$, velocity $\mathbf{v}_p$, mass m_p, density ρ_p, stress tensor $\boldsymbol{\sigma}_p$, strain tensor $\boldsymbol{\varepsilon}_p$ and all other internal state variables necessary for the constitutive model, where p is the index of the particle. At each time step, the mass and velocities of the material particles are mapped onto the background computational mesh. The mapped momentum at node i is obtained by $m_i\mathbf{v}_i = \sum_p m_p\mathbf{v}_p N_i(\mathbf{x}_p)$, where N_i is the element shape function and the nodal mass m_i reads

$m_i = \sum_p m_p N_i(\mathbf{x}_p)$. Suppose that a computational mesh is constructed of eight-node cells for three-dimensional problems; then the shape function is defined as

$$N_i = \tfrac{1}{8}(1 + \xi\xi_i)(1 + \eta\eta_i)(1 + \varsigma\varsigma_i), \tag{1}$$

where ξ, η, ς are the natural coordinates of the material particle in the cell along the x-, y-, and z-directions, respectively; ξ_i, η_i, ς_i take corresponding nodal values ± 1. The mass of each particle is equal and fixed, so the mass conservation equation, $\mathrm{d}\rho/\mathrm{d}t + \rho\nabla \cdot \mathbf{v} = 0$, is automatically satisfied.

For pure mechanical problems the differential equation of balance reads

$$\rho\, \mathrm{d}\mathbf{v}/\mathrm{d}t = \nabla \cdot \boldsymbol{\sigma} + \rho\mathbf{b}, \tag{2}$$

where ρ is the mass density, $\mathbf{v}$ the velocity, $\boldsymbol{\sigma}$ the stress tensor and $\mathbf{b}$ the body force. The momentum equation is solved on a finite-element mesh in a Lagrangian frame. The weak form of it can be found, based on the standard procedure:

$$\int_\Omega \rho\delta\mathbf{v} \cdot \mathrm{d}\mathbf{v}/\mathrm{d}t\, \mathrm{d}\Omega + \int_\Omega \delta(\mathbf{v}\nabla) \cdot \boldsymbol{\sigma}\, \mathrm{d}\Omega - \int_{\Gamma_t} \delta\mathbf{v} \cdot \mathbf{t}\, \mathrm{d}\Gamma - \int_\Omega \rho\delta\mathbf{v} \cdot \mathbf{b}\, \mathrm{d}\Omega = 0. \tag{3}$$

Since the continuous body is described with the use of a finite set of material particles, the mass density can be written as $\rho(\mathbf{x}) = \sum_{p=1}^{N_p} m_p \delta(\mathbf{x} - \mathbf{x}_p)$, where δ is the Dirac delta function with dimension of the inverse of volume. The substitution of $\rho(\mathbf{x})$ into the weak form of the momentum equation converts the integral to the sums of quantities evaluated at the material particles, namely,

$$m_i\, \mathrm{d}\mathbf{v}_i/\mathrm{d}t = (\mathbf{f}_i)^{\mathrm{int}} + (\mathbf{f}_i)^{\mathrm{ext}}, \tag{4}$$

where the internal force vector is given by $\mathbf{f}_i^{\mathrm{int}} = -\sum_p^{N_p} m_p \boldsymbol{\sigma}_p \cdot (\nabla N_i)/\rho_p$, and the external force vector reads $\mathbf{f}_i^{\mathrm{ext}} = \sum_{p=1}^{N_p} N_i \mathbf{b}_p + \mathbf{f}_i^{\mathrm{c}}$, where the vector $\mathbf{f}_i^{\mathrm{c}}$ is the contacting force between two bodies. In the present paper, all colliding bodies are composed of the same material, and $\mathbf{f}_i^{\mathrm{c}}$ is treated in the same way as the internal force.

The nodal accelerations are calculated by equation (4) with an explicit time integrator. The critical time step satisfying the stability conditions is the ratio of the smallest cell size to the wave speed. Once the motion equations are solved on the cell nodes, the new nodal values of acceleration are used to update the velocity of the material particles. The strain increment for each material particle is determined using the gradient of the nodal basis function evaluated at the position of the material particle. The corresponding stress increment can be found from the constitutive model. The internal state variables can also be completely updated. The computational mesh may be the original one or a newly defined one, chosen for convenience, for the next time step. More details of the algorithm are given in [22, 23].

3. Physical model

We consider an associative von Mises plasticity model with linear kinematic and isotropic hardening [24]. Introducing a linear isotropic elastic relation, the volumetric plastic strain is zero, leading to a deviatoric–volumetric decoupling. So, it is convenient to split the stress and strain tensors, $\boldsymbol{\sigma}$ and $\boldsymbol{\varepsilon}$, as

$$\boldsymbol{\sigma} = \mathbf{s} - P\mathbf{I}, \qquad P = -\tfrac{1}{3}\mathrm{Tr}(\boldsymbol{\sigma}), \tag{5}$$

$$\boldsymbol{\varepsilon} = \mathbf{e} + \tfrac{1}{3}\theta\mathbf{I}, \qquad \theta = \tfrac{1}{3}\mathrm{Tr}(\boldsymbol{\varepsilon}), \tag{6}$$

where P is the pressure scalar, $\mathbf{s}$ the deviatoric stress tensor, and $\mathbf{e}$ the deviatoric strain. The strain $\mathbf{e}$ is generally decomposed as $\mathbf{e} = \mathbf{e}^{\mathrm{e}} + \mathbf{e}^{\mathrm{p}}$, where $\mathbf{e}^{\mathrm{e}}$ and $\mathbf{e}^{\mathrm{p}}$ are the traceless elastic and

plastic components, respectively. The material shows a linear elastic response until the von Mises yield criterion,

$$\sqrt{\tfrac{3}{2}}\|\mathbf{s}\| = \sigma_{\mathrm{Y}}, \tag{7}$$

is reached, where σ_{Y} is the plastic yield stress. The yield σ_{Y} increases linearly with the second invariant of the plastic strain tensor $\mathbf{e}^{\mathrm{p}}$, i.e.,

$$\sigma_{\mathrm{Y}} = \sigma_{\mathrm{Y0}} + E_{\tan}\|\mathbf{e}^{\mathrm{p}}\|, \tag{8}$$

where σ_{Y0} is the initial yield stress and $E_{\tan}$ the tangential module. The deviatoric stress $\mathbf{s}$ is calculated by

$$\mathbf{s} = \frac{E}{1+\nu}\mathbf{e}^{\mathrm{e}}, \tag{9}$$

where E is Young's modulus and ν Poisson's ratio. Denote the initial material density and sound speed by ρ_0 and c_0, respectively. The shock speed U_{s} and the particle speed U_{p} after the shock follow a linear relation, $U_{\mathrm{s}} = c_0 + \lambda U_{\mathrm{p}}$, where λ is a characteristic coefficient of the material. The pressure P follows the Mie–Grüneisen equation of state:

$$P = (C\mu + D\mu^2 + S\mu^3)\left(1 - \frac{\gamma\mu}{2}\right) + \gamma\rho\epsilon, \tag{10}$$

where ϵ is the internal energy, $\mu = \rho/\rho_0 - 1$, $\gamma = \gamma_0\rho_0/\rho$, $C = \rho_0 c_0^2$, $D = C(2\lambda - 1)$, $S = C(\lambda - 1)(3\lambda - 1)$. In this paper the material used is aluminium. The corresponding parameters are $\rho_0 = 2700$ kg m^{-3}, $E = 69$ MPa, $\nu = 0.33$, $\sigma_{\mathrm{Y0}} = 120$ MPa, $E_{\tan} = 384$ MPa, $c_0 = 5.35$ km s^{-1}, $\lambda = 1.34$, and $\gamma_0 = 1.96$ when the pressure is below 270 GPa [25].

Before the numerical experiments, we validated our code by several benchmark simulations. The first one involves a cylinder rolling on an inclined rigid plane. The second involves the collision of two elastic spheres. The third involves a copper Taylor bar impacting to a rigid wall. The fourth is to simulate the process of the collision between four identical spheres. All the simulation results agree well with the analytic or experimental ones [22].

In our numerical experiments the shock wave to the target material is loaded via either of two equivalent means, impacting with another body in the vertical direction or by a rigid wall at the bottom. The horizontal boundaries are treated as rigid walls. The initial configuration of the material particles is set to be symmetric about the central vertical line. Such a configuration corresponds also to a real system composed of many of the simulated ones aligned periodically in the horizontal direction. In this paper we focus on the two-dimensional simulations.

4. Results of numerical experiments

As the first step, we set a single cavity in the metal material. Due to the boundary conditions mentioned above, such a simulation model corresponds also to a very wide system with a row of cavities in it. We study various cases where the shock wave changes from strong to weak. In the cases with strong shock, we concern ourselves with the jet creation and the distribution of the 'hot spots'. When the cavity is close to the free surface, we check whether or not there is material ejected out of the free surface. In the cases with weak shock, we study the effects of cavity size, distance from the cavity centre to the impacting face, the initial yield stress of the material, etc, on the collapsing procedure.

Figure 1 shows a snapshot for a case with very high impacting speed. The width of the simulated system is 10 μm. Two metal bodies with symmetric configurations collide. The speed of each is 1500 m s^{-1}. That is to say, the relative impacting speed is 3000 m s^{-1}. Thus, the initial pressure on one body loaded by the shock is about 30 GPa, being less than the critical

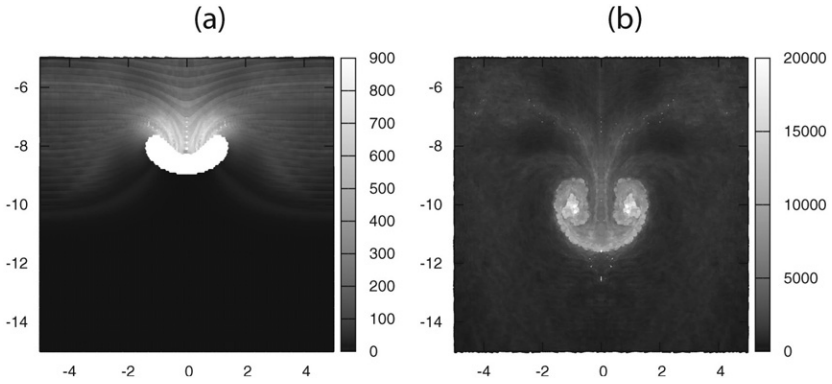

Figure 1. Snapshots of collapse of a single cavity under strong shocks. From black to white the grey level in the figure shows the increase of local temperature denoted by the plastic work during the deformation procedure. The spatial unit is the micrometre. The unit of work is the millijoule. (a) $t = 2$ ns, (b) $t = 5$ ns.

value, 270 GPa. The global procedure can be described as follows. (i) When the shock wave arrives at the upper-stream wall of the cavity, plastic deformation begins to occur. The shock waves at the two sides of the cavity move forwards to the free surface. The shock speed at the two sides is larger than the deforming speed of the upper-stream wall of the cavity. (ii) The upper-stream wall continues its collapse, and a configuration with a turned 'C' shape appears. The material projected into the cavity makes a jet. A 'hot spot' occurs at the tip region of the jet. (See figure 1(a).) (iii) The speed of the jet increases with time. The tip of the jet catches up, then overtakes the shock waves at its two sides. (iv) The jetted material impacts the downstream wall of the cavity, resulting in a pair of vortices rolling in opposite directions. The 'hot spots' appear at the centres of the vortices. (See figure 1(b).)

In the case where the cavity locates near the upper free surface, if the shock wave is strong enough, the material projected into the cavity will become a jet and hit the downstream wall and break it. This procedure makes another dynamical picture of ejection by shock. Such a behaviour has been observed in experiments and has some potential applications. We show such a dynamical procedure in figure 2, where the shock wave is loaded by colliding with rigid bottom wall. The simulated system here is 10 μm in width. The initial radius of the cavity is 1.5 μm. The distance between the cavity centre to the upper free surface is 4.5 μm. The impacting speed of the metal body to the rigid wall is 1120 m s^{-1}. The corresponding times in figures 2(a)–(f) are 1.2 ns, 1.4 ns, 2.0 ns, 2.4 ns, 4.4 ns, and 12.0 ns, respectively. Figure 2(a) shows a snapshot where the shock wave has passed the majority of the cavity. The upper-stream part of cavity has been substantially deformed and some material have been projected into the cavity. Up to the time $t = 1.6$ ns, as shown in figure 2(b), the cavity has been nearly filled with the jetted material; a compressive wave is arriving at the free surface from the two sides and rarefactive waves will be reflected back. The reflected rarefactive waves decrease the pressure in the influenced region and cavitation occurs around the region of the original cavity and at the two sides of the jet path. (See figures 2(c) and (d).) Compared with that at the two sides, the material in the middle is at a much higher pressure and has much more pronounced kinetic energy, so it is significantly distorted. The newly created cavities coalesce and become larger with time. (See figure 2(e).) If the upper wall of the newly created cavity possesses enough kinetic energy, it will be broken. (See figure 2(f).) Figure 3 shows the corresponding configurations with temperature. In figure 3(a) the temperature of the

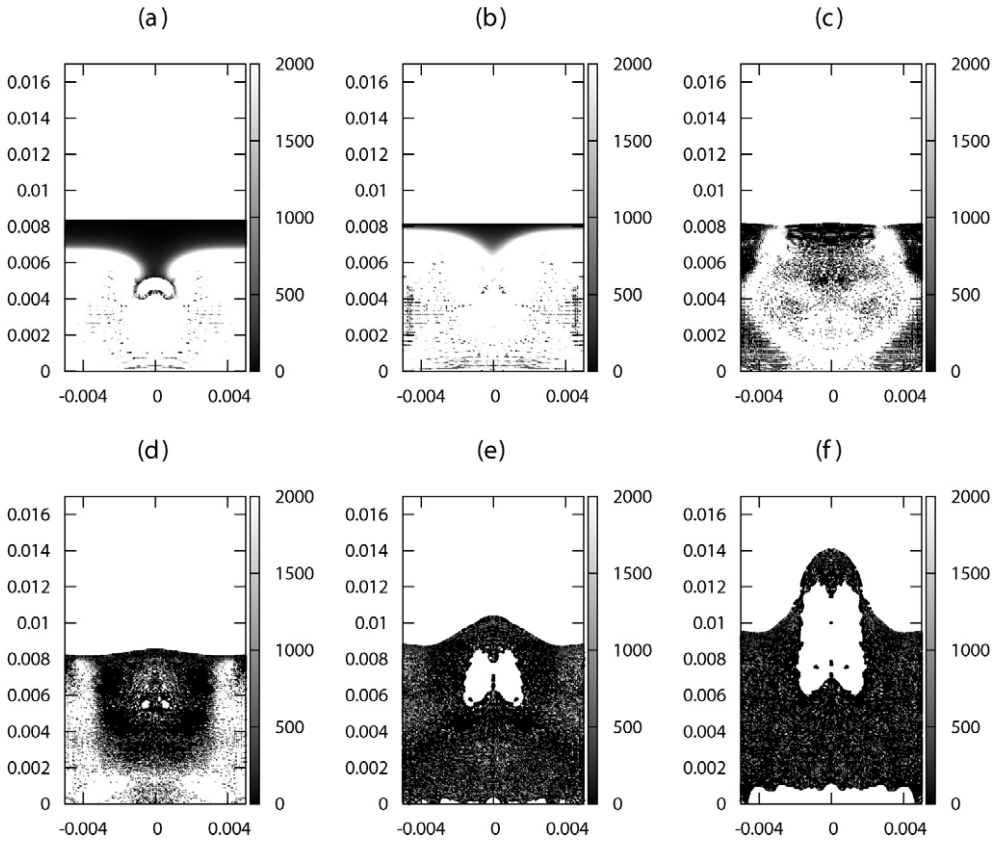

Figure 2. Snapshots of collapse of a single cavity under a strong shock. For the pressure contour, from black to white the value increases. The corresponding times for (a)–(f) are 1.2, 1.6, 1.8, 2.0, 2.2, 12 ns, respectively. The spatial unit is the millimetre. The unit of pressure is the megapascal.

compressed region around the cavity is higher that in other regions. The 'hot spot' is at the tip of the metal tongue. In figures 3(b) and (c) the 'hot spot' occurs at the regime hit by the metal tongue. After the appearance of the new cavity, 'hot spots' locate at the inner wall of the cavity, especially the upper and bottom walls. (See figures 3(d)–(f).) Whether or not there is metal material ejected from the upper free surface depends on the initial impacting speed u and the width of the upper wall of the original cavity d. The critical impacting speed u increases parabolically with d. Figure 4 shows the simulation results and fitting curve.

With the decrease of impact speed, the collapse becomes slower. When the impact speed decreases to about 200 m s^{-1}, the dynamical picture is significantly different: the cavity cannot be collapsed completely, and the final configuration around the cavity varies from (nearly) symmetric to asymmetric if we change the distance from the cavity centre to the impacting surface. In figure 5 we show an 'abnormal' asymmetric dynamical picture where the cavity collapsed less in the initial shock direction. Here the width of the simulated system is 10 μm. The initial radius of the cavity is 1.5 μm. The distance between the cavity centre and the impact surface of the metal body is 1.9 μm. To understand the observed behaviour, we 'recover' or 'magnify' the system in the following way: the rigid walls at the two sides and at the bottom of the computational region can be regarded as 'mirrors'. In other words, the system is symmetric about the 'mirrors'. The distance between two successive cavities in the horizontal direction is

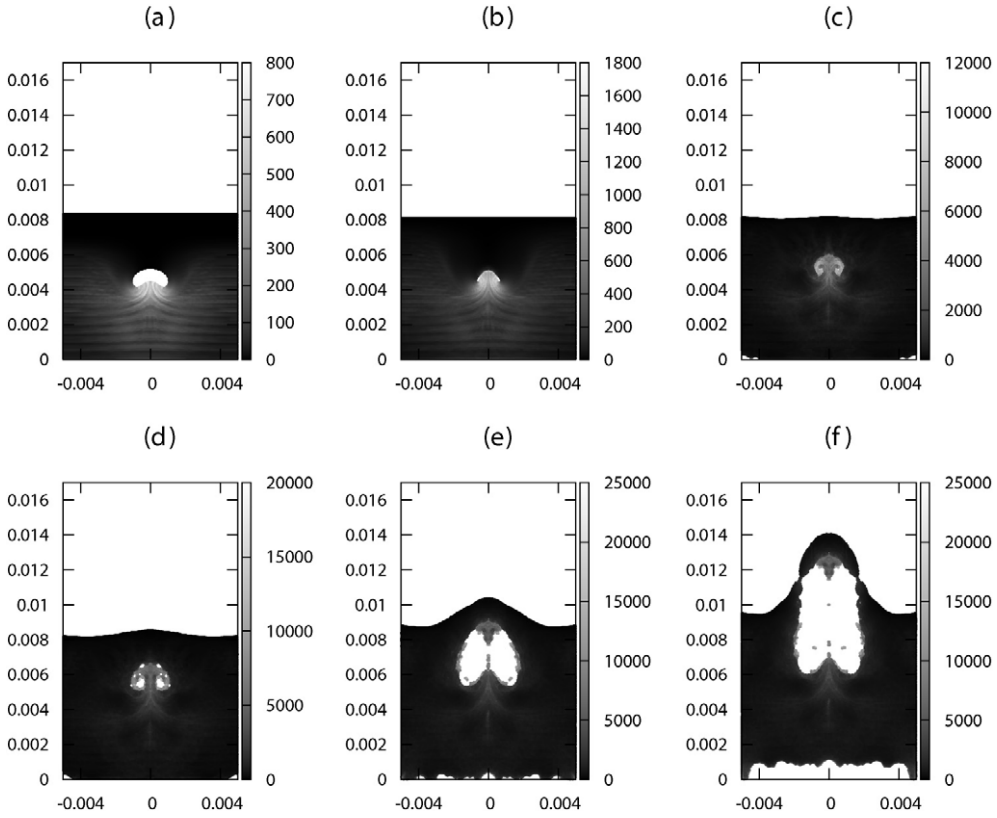

Figure 3. Configurations with local temperature denoted by the plastic work during the deformation. The unit of work is the millijoule. Parts (a)–(f) here correspond to parts (a)–(f) in figure 2, respectively.

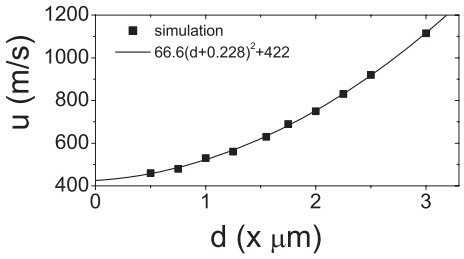

Figure 4. Critical impact velocity versus the thickness of the downstream wall of the cavity. The symbols are simulation results and the solid line is the fitting result.

$d_{\mathrm{H}} = 10\ \mu$m, while the distance between the cavity in the computed body and the fictitious one symmetric about the impacting face is $d_{\mathrm{V}} = 3.8\ \mu$m. The cavities reflect rarefactive waves. Therefore, the pressure in between decreases. Since the distance d_{V} in the vertical direction is much less than d_{H} in the horizontal direction, the rarefactive waves in between the two cavities in the vertical direction are reflected more frequently. Correspondingly, the pressure in this region is much lower than that in the surrounding region. This results in less collapsing of the lower part of the cavity. When the shock waves arrive at the upper free surface, rarefactive

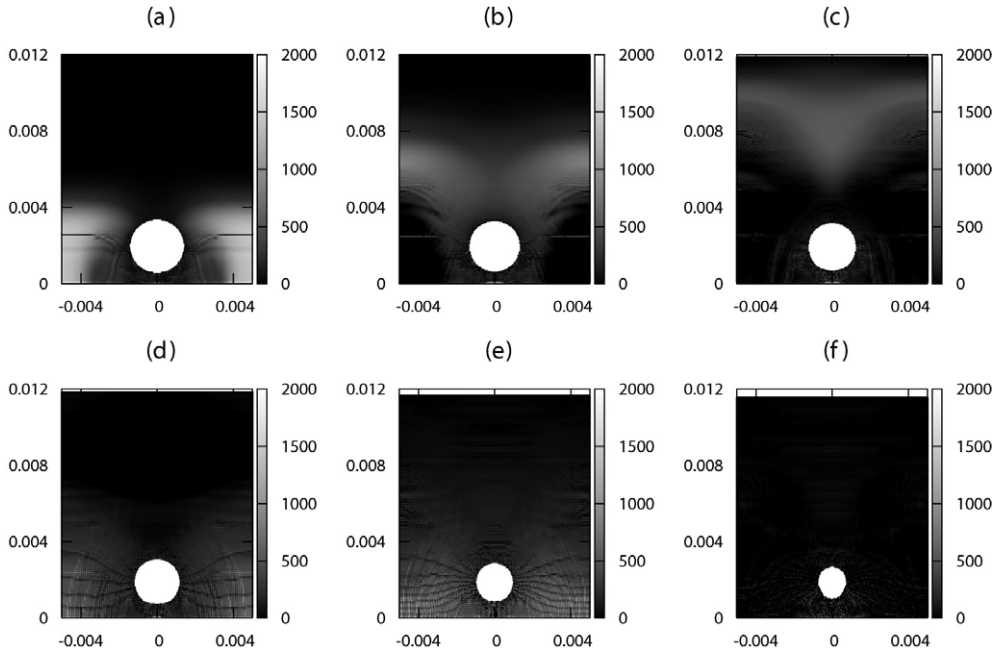

Figure 5. Snapshots of collapse of a single cavity under a weak shock. From black to white the grey level in the figure shows the increase of local pressure. The spatial unit is the millimetre. The unit of pressure is the megapascal. (a) $t = 1.0$ ns, (b) $t = 1.6$ ns, (c) $t = 2.2$ ns, (d) $t = 3.0$ ns, (e) $t = 5.4$ ns, (f) $t = 16.0$ ns.

waves are reflected back towards the cavity. This is a second reason for the cavity to collapse less in the vertical direction. Compared with those from the fictitious cavity below the bottom, the reflected rarefactive waves from the upper free surface are much wider. This explains why the collapsing of the lower part of the cavity is more pronounced. Figure 6 shows the corresponding configurations with temperature. The hottest region appears in the region below the cavity. In figures 5 and 6, parts (a)–(f) correspond to 1.0 ns, 1.62 ns, 2.2 ns, 3.0 ns, 5.4 ns and 16 ns, respectively. From figures 5(a) and 6(a) it is clear that, around this time, although the rarefactive wave decreased the pressure within the influenced region, the temperature there is higher than in other parts of the system. The reason is that the waves there did more plastic work. Since the cavity here corresponds to a vacuum, pure fluidic models are not able to capture such a phenomenon.

The temperature in the 'hot spot' increases in the course of collapsing. If we further decrease the distance between the cavity and the lower impacting face, the lower part of the cavity will be collapsed more pronouncedly. Figure 7(a) shows the final steady state for a case where the lower boundary of the cavity just locates at the impacting face. In contrast, if we increase the distance, the collapsed cavity will be more symmetric. Figure 7(b) shows a case where the collapsing is nearly isotropic.

We studied cases with various sizes of cavity. It is found, for the investigated cases, that the collapsibility becomes larger when the initial size of the cavity is reduced. The variation of area of the cavity with time is shown in figure 8(a), where four kinds of radius are used. They are 2.5 μm, 2.0 μm, 1.5 μm, and 1 μm, respectively. If we define the collapsibility as $\Phi = (A_0 - A)/A_0$, then it is clear that Φ decreases as the cavity becomes larger, where A_0 and A are the areas of the cavity in the initial and final states. (See figure 8(b).) In order to study the

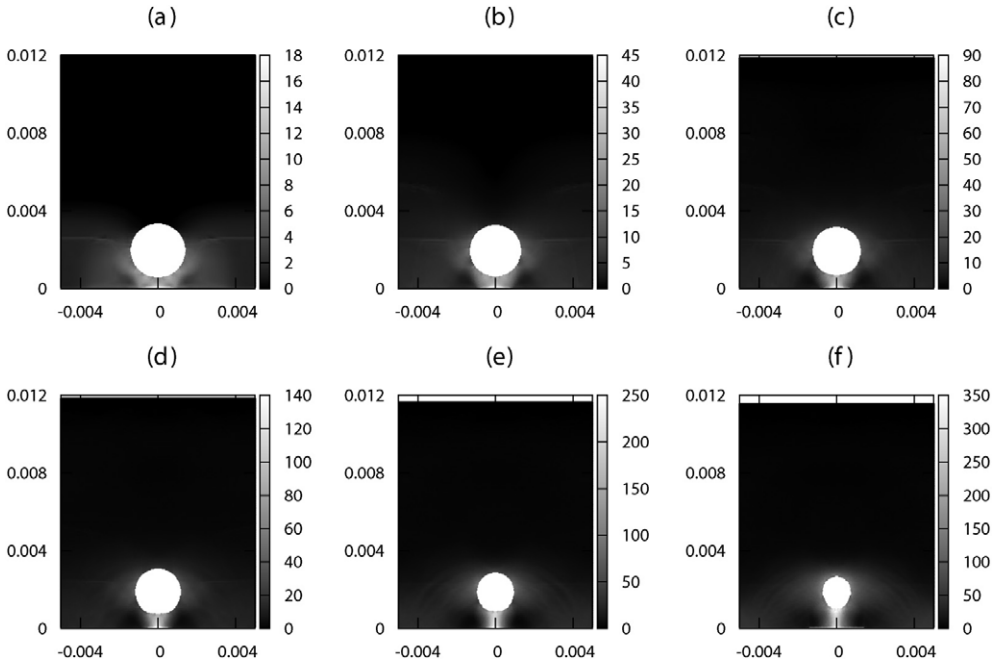

Figure 6. Configurations with local temperature denoted by the plastic work during the deformation. The unit of work is the millijoule.

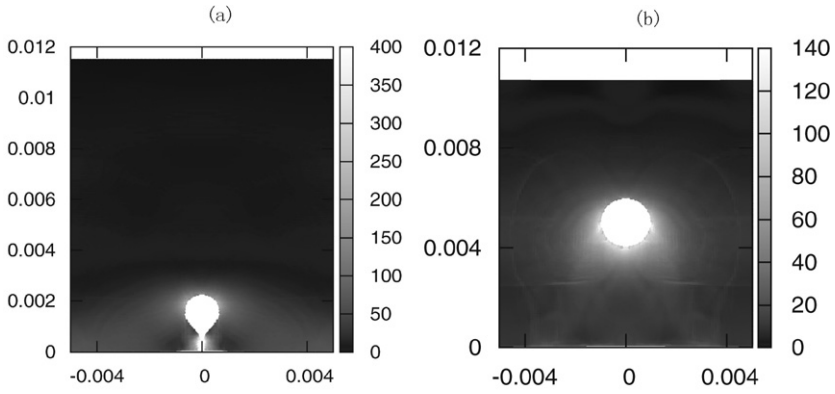

Figure 7. Transition of symmetry of collapsing. (a) Asymmetric in the vertical direction near the impacting face; (b) nearly symmetric collapse. The grey level in the figure corresponds to the plastic work. The spatial unit in the figure is the millimetre. The unit of energy is the millijoule.

effect of individual material characteristics on the collapsing procedure separately, we changed the initial yield stress of the material under the condition that all other parameters are fixed. The corresponding collapsing procedures are shown in figure 8(c), where the numbers in the legend indicate the initial yield stresses used. The unit is the megapascal. Figure 8(d) shows that the collapsibility decreases parabolically if the initial yield becomes larger.

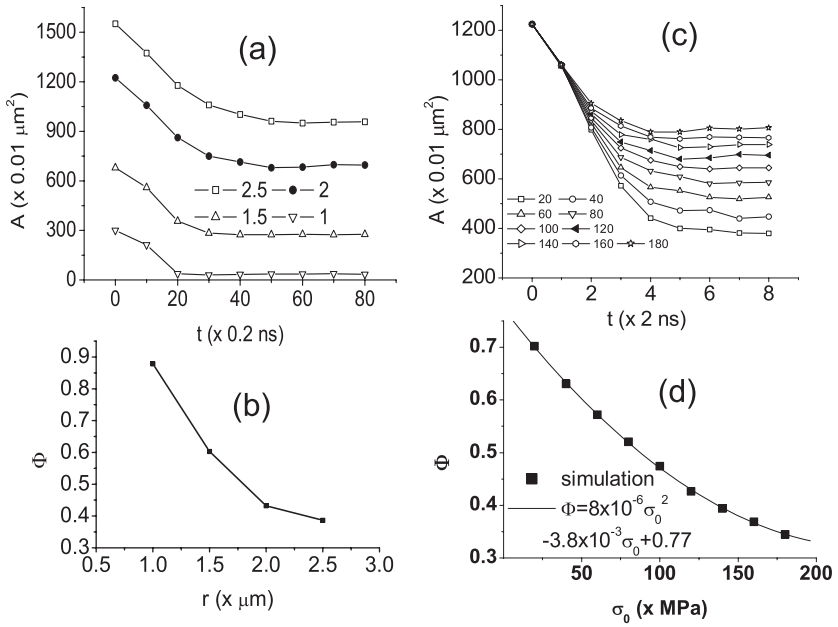

Figure 8. Effects of cavity size ((a) and (b)) and initial yield ((c) and (d)) to the collapsing procedure. (a) Area of cavity versus time for different initial radius. Shown in the legend are the initial radii; the unit is the micrometre. (b) Collapsibility versus initial radius of cavity. (c) Area of cavity versus time for different initial yield stresses. Shown in the legend are the initial yield stresses; the unit is the megapascal. (d) Collapsibility versus initial yield stress.

5. Conclusion

The collapse of cavities under shock is investigated by the material-point method. What the present paper mainly concerned includes behaviours ignored by pure fluidic models and those quick distortion procedures which are generally difficult for the traditional finite-element method [18]. We studied the relations between symmetry of collapsing and the strength of shock, and other coexisting interfaces, as well as hydrodynamic and thermal–dynamic behaviours. In the case with strong shock, the procedure of jet creation in the cavity was studied. The jetted material hits the downstream wall and results in two vortices rolling in opposite directions. The 'hot spots' occur in the two centres of vortices. When the shock is strong enough, the jet material with high kinetic energy hits and breaks the downstream wall. The critical impact speed for such a phenomenon increases parabolically with the thickness of the downstream wall. In the case with weak shock, it was found that the cavity cannot collapse completely and that it may collapse in a nearly isotropic way. The transition of symmetry in the course of collapsing is related to the size of the cavity, and the distances to the walls, as well as the impacting speed, etc. The distribution of 'hot spots' in the shocked material changes for different collapsing procedures. Since we use the Mie–Grüneisen equation of state and the effects of strain rate are not taken into account, the behaviour is the same if the spatial and temporal scales are magnified in the same way. The results obtained in the paper will help to understand better the course of ignition of inhomogeneous explosives, fatigue and erosion of metal materials, etc.

Acknowledgments

We warmly thank S G Bardenhagen, Haifeng Liu, Shigang Chen, Yingjun Li, Song Jiang, Xingping Liu, Xijun Yu, Zhijun Shen, Yangjun Ying, Guoxi Ni, and Yun Xu for helpful discussions. We acknowledge support by the Science Foundation of Laboratory of Computational Physics, IAPCM, the National Science Foundation of China (No. 10472052) and the National Basic Research Program of China (No. 2002BC412701).

References

[1] Reynolds O 1894 *Sci. Pap.* **2** 587
[2] Silberrad D 1912 *Engineering* 34
Ramsay W 1912 *Engineering* 687
[3] Kornfeld M and Suvorov L 1944 *J. Appl. Phys.* **15** 495
[4] Brennen C E 1995 *Cavitation and Bubble Dynamics* (Oxford: Oxford University Press)
[5] Bourne N K 2002 *Shock Waves* **11** 447
[6] Saito Y and Sato K 2003 *CAV2003: 5th Int. Symp. on Cavitation (Osaka, Nov. 2003)* Cav03-GS-11-004
Tanguay M and Colonius T 2003 *CAV2003: 5th Int. Symp. on Cavitation (Osaka, Nov. 2003)* OS-2-1-010
[7] Hansson I, Kedrinskii V and Morch K A 1982 *J. Phys. D: Appl. Phys.* **15** 1725
[8] Hansson I and Morch K A 1980 *J. Appl. Phys.* **51** 4651
[9] Shapiro V D *et al* 1993 *Phys. Fluids* **5** 3148
[10] Putterman S J 1995 *Sci. Am.* **272** 46
Barbaglia M O and Bonetto F J 2004 *J. Appl. Phys.* **95** 1756
[11] Song W D, Hong M H, Lukyanchuk B and Chong T C 2004 *J. Appl. Phys.* **95** 2952
[12] Wrigley D M and Llorca N G 1992 *J. Food Prot.* **55** 678
[13] Sass W, Braunlich M, Deyer H P, Matura E, Folberth W, Priemeyer H G and Seifert J 1991 *Ultrasound Med. Biol.* **17** 239
[14] Palanker D, Vankov A and Miller J 2003 *J. Appl. Phys.* **94** 2654
[15] Zhao Y H, Li Y J, Yang Z A and Zhang G 2006 *Chin. J. Comput. Phys.* **23** 343 (in Chinese)
[16] Yang Q L, Zhang G, Xu A, Zhao Y H and Li Y J 2007 *Acta Phys. Sin.* at press (in Chinese)
[17] Srinivasan S G, Baskes M I and Wagner G J 2007 *J. Appl. Phys.* **101** 043504
[18] Niordson C F and Tvergaard V 2007 *Modelling Simul. Mater. Sci. Eng.* **15** S51
[19] Rayleigh L 1917 *Phil. Mag.* **34** 94
Hickling R and Plesset M S 1964 *J. Fluid Mech.* **7** 7
[20] Harlow F H 1964 *Methods for Computational Physics* vol 3, ed B Adler, S Fernbach and M Rotenberg (New York: Academic) pp 319–43
[21] Burgess D, Sulsky D and Brackbill J U 1992 *J. Comput. Phys.* **103** 1
Sulsky D, Chen Z and Schreyer H L 1994 *Comput. Methods Appl. Mech. Eng.* **118** 179
Sulsky D, Zhou S J and Schreyer H L 1995 *Comput. Phys. Commun.* **87** 236
Sulsky D and Schreyer H L 1996 *Comput. Methods Appl. Mech. Eng.* **139** 409
[22] Pan X F, Xu A and Zhang G 2007 *GF Report of China (No. GF-A0093306G)* (in Chinese)
[23] Ma S 2005 Material point method for 3D hypervelocity impact simulation *Master Thesis* Tsinghua University, Beijing (in Chinese)
[24] Auricchio F and da Veiga L B 2003 *Int. J. Numer. Methods Eng.* **56** 1375
[25] Meyers M A 1994 *Dynamic Behavior of Materials* (New York: Wiley)